Downloaded 12/02/14 to 205.196.179.237. Redistribution subject to SEG license or copyright; see Terms of Use at http://library.seg.org/

An application of FWI to deep water Hernando NAZ streamer data in Gulf of Mexico

Kwangjin Yoon, Ioan Vlad, Peyman Moghaddam, Jian Mao, and Jianming Sheng, TGS*

Summary

We applied Full Waveform Inversion (FWI) to a karst and gas chimney area from Hernando 3D Narrow-Azimuth (NAZ) deep-water streamer data in the Gulf of Mexico. Karst distributes locally and has low velocity and large velocity contrast against surrounding sediments. FWI is an attractive tool for velocity modeling in this area. FWI detected a low-velocity karst zone which matches the Kirchhoff image. The convergence of FWI was confirmed by comparing seismograms and phases between observed and synthetic data. FWI improved the depth migration image quality and the flatness of common image gathers.

Introduction

This is a case study for FWI application to a NAZ streamer dataset acquired in deep water Gulf of Mexico. The subsurface of the survey area contains karst in the depth range of 2 km to 3 km. Generally, karst has lower velocity than surrounding sediments and the velocity contrast is quite large. Karst is distributed in local features a few meters to a few hundred meters in size and causes strong diffractions which contaminate the seismic image. Tomographic velocity modeling is not able to fully resolve the karst structures. The ability of FWI to produce high resolution velocity makes it a suitable tool for resolving complex low-velocity anomalies such as karst. We applied FWI to this dataset to study the feasibility of FWI as a small-velocity anomaly-detection method and to determine an effective workflow for deep-water streamer data. We describe the FWI workflow step-by-step from data preparation and source estimation to depth imaging using the final FWI velocity.

The FWI algorithm developed by Lailly (1983) and Tarantola (1984) reduces misfit between observed and synthetic data and converges to a local minimum. Other workflows may cause the inversion procedures to converge to different local minima. Therefore it is important to study what type of workflow is effective for a particular dataset. Unlike OBN and OBC data, in streamer data, each shot covers a small area and the physical conditions for source-wavelet generation and receiver-signal acquisition are not the same for all of the traces in one bin. These conditions make streamer-data FWI require denser shot spacing and more iterations than the FWI using datasets with fixed receivers. Data acquired in deep water lack the transmitted early arrivals. It means the FWI gradient has insufficient low-wavenumber components for a background velocity update. In this case, we can use a scheme to do FWI with turning waves and large reflection angle events first (Sheng et al., 2006) and gradually include narrower reflection angle signals by applying various muting functions to the input.

Preprocessing and source estimation

We selected a 4 km by 24 km in the karst area on the shelf from Hernando dataset to test FWI. The streamer dataset in the selected area has 4 sail lines for a total of 2051 shots. Shot and receiver intervals are 37.5 m and 12.5 m. The streamer length is 7.5 km. FWI used every 3rd or 4th shot and every 5th receiver. This source and receiver decimation and total recording time reduction from 14 s to 7 s reduced the size of FWI input data from 200 GB to 20 GB. The sea bottom is not flat and has a depth range of 0.8 km ~ 1.5 km. A low-pass filter of 0 to 8 Hz was applied to the data. Figure 1(a) shows one filtered shot gather sorted by absolute offset. Deghosting and demultiple were not applied to the input.

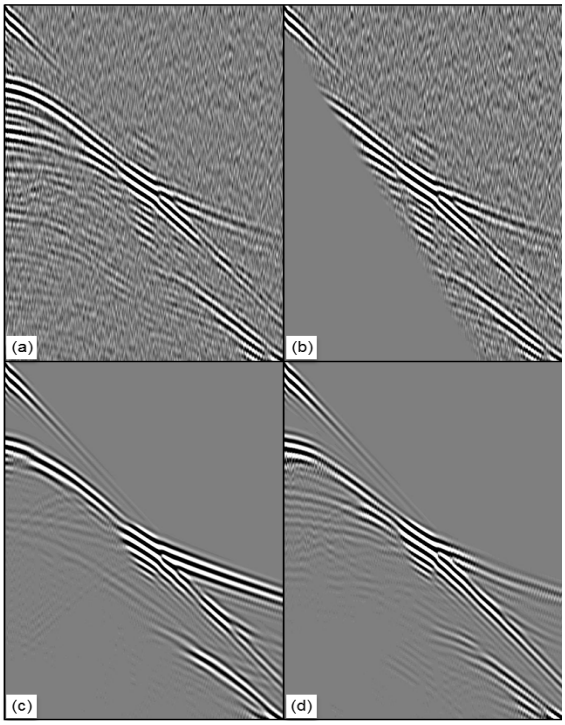

Figure 1. Shot gathers sorted in offset distance. Maximum offset and recording time are 7.5 km and 7 s. (a) Input, after low pass filter and 500 ms static shift, (b) after muting with a linear function of 6000 m at 7 s, (c) synthetic seismogram at starting velocity and (d) synthetic seismogram after FWI.

© 2014 SEG

DOI http://dx.doi.org/10.1190/segam2014-1611.1

Downloaded 12/02/14 to 205.196.179.237. Redistribution subject to SEG license or copyright; see Terms of Use at http://library.seg.org/

The source wavelet was estimated from the near offset using a near-offset stack and updating it in frequency domain (Yoon et al., 2014). The low-pass filtered input data were shifted down for a causal wavelet. And then the traces were aligned using the surface velocity and the near-offset traces were stacked to estimate an initial source wavelet S_0. A new source wavelet S_{new} was updated from the initial source wavelet using observed data D and synthetic data U generated from S_0 based on the frequency domain source estimation method described by Pratt (1999):

$$S_{new}(\omega) = S_0(\omega)(\sum D(\omega)U(\omega)^* / \sum U(\omega)U(\omega)^*). \quad (1)$$

Figure 1(c) and 1(d) are synthetic seismograms generated by the updated source wavelet based on the starting velocity and the velocity driven by FWI.

Inversion

In FWI, we use the anisotropic VTI acoustic wave equation with a free-surface boundary condition. Anisotropic parameters ε and δ were fixed and only the vertical velocity was updated. Each trace in the observed and the synthetic data has been normalized for a phase-only inversion. Deghosting and demultiple were not applied to the input. However the input was muted with a simple muting function. Figure 1(b) displays the input muted by a linear function to 6000 m at 7 s. We began the FWI with the transmitted early arrivals to update the lowest wavenumber velocity structure first. After the first FWI, additional iterations of FWI were run sequentially with different inputs including the FWI velocity generated at the previous inversion stage. The inputs to the 2nd and 3rd rounds of FWI were generated by muting functions to 4000 m at 7 s and 0 m at 7 s respectively to include more reflection events in the inversion process. This multi-stage FWI gradually added high wavenumber structures to the velocity model.

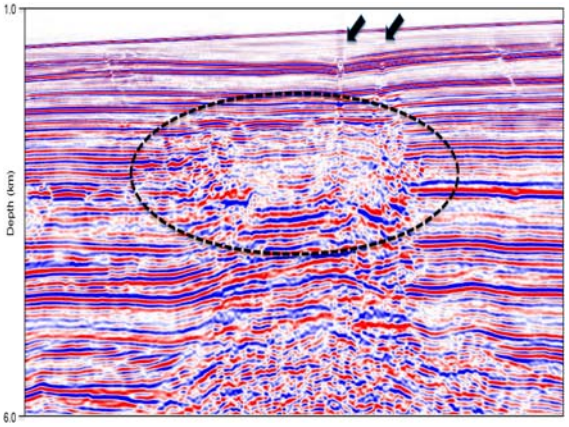

Figure 2. Kirchhoff depth migration image using the starting velocity in Figure 3(a). We believe the poor image around 2 km ~ 3 km depth is caused by Karst which may exist in the black dashed circle. The vertical image anomaly indicated by black arrows seem to be caused by low velocity gas chimneys.

Figure 2 shows the Kirchhoff depth migration image using the starting velocity model shown in Figure 3(a). Based on the geologic interpretation, this area has karst structures around the depth range of 2 km ~ 3km. The karst is believed to have a lower velocity than the surrounding rocks and to cause severe diffractions of the seismic waves. The dashed black circle in Figure 2 denotes the potential area where the karst may exist. The karst degrades the image of mid depth and below. The two black arrows in Figure 2 are interpreted as gas leakages. The goal of FWI is to detect the low-velocity karst zone.

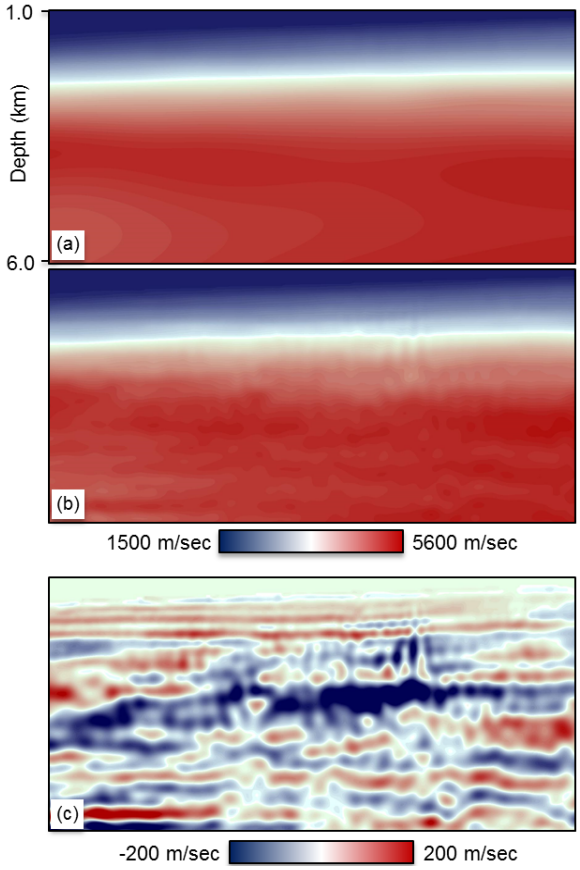

Figure 3. Vertical profiles of (a) velocity before FWI, (b) velocity after FWI and (c) velocity perturbation produced by FWI. Low velocity anomalies in Figure 3(c) match the locations of the potential karst area and gas leakages shown in Figure 2.

© 2014 SEG

DOI http://dx.doi.org/10.1190/segam2014-1611.1

Downloaded 12/02/14 to 205.196.179.237. Redistribution subject to SEG license or copyright; see Terms of Use at http://library.seg.org/

A total of four (4) frequency bands centered at 4.2 Hz, 5 Hz, 6 Hz and 7.3 Hz were used in FWI iterations. Figure 3 shows vertical profiles of (a) starting FWI velocity, (b) velocity after multi stage FWI runs and (c) the velocity perturbation produced by FWI. This velocity update detected by FWI shows a low velocity area which coincides with the poor image zone indicated by the dashed circle in Figure 2. Although the resolution is not good, vertical low-velocity anomalies can be identified at the location of the gas leakages indicated by black arrows in Figure 2.

Figure 4 displays horizontal slices at 1720 m depth of (a) Kirchhoff depth image, (b) the starting FWI velocity, (c) the velocity after 2nd FWI round using input muted by function of 4000 m over 7 s and (d) the final FWI velocity acquired after the 3rd inversion. As shown in Figure 4, transmitted wave updated the low wavenumber background velocity and higher wavenumber structures were added to the velocity as the input includes gradually more and more reflection events. The locations of low-velocity anomalies that appear as dot shapes in Figure 4(d) match the structure of the Kirchhoff depth slice shown in Figure 4(a).

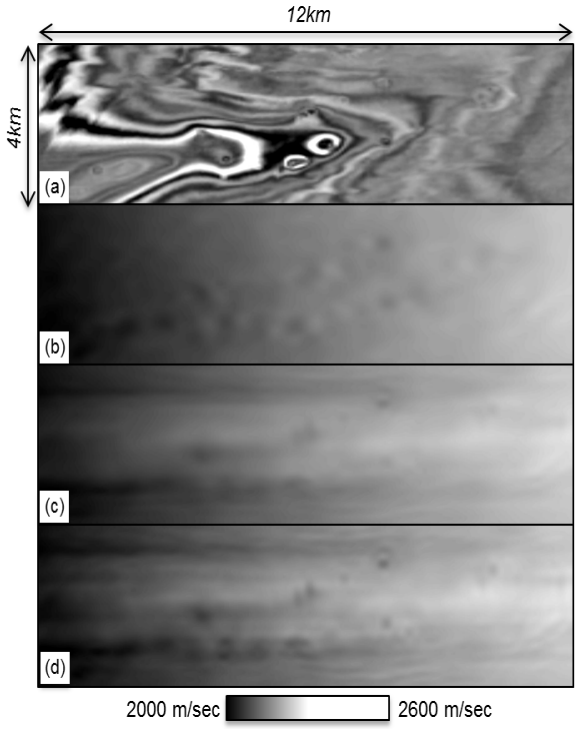

Figure 4. Depth slices at the depth of 1720 m (a) Kirchhoff depth image, (b) starting FWI velocity, (c) FWI velocity after 2nd stage using input muted by a function of 4000 m over 7 s and (d) FWI velocity after the 3rd FWI.

Quality and convergence control

FWI convergence can be confirmed by several tools. We used four tools to compare initial and FWI velocities: 1) Kirchhoff depth migration images, 2) Kirchhoff depth migration image gathers, 3) synthetic seismograms, and 4) phase residuals (Warner et al., 2013). Figure 1(a) and 1(d) are an offset-sorted input shot gather and its corresponding synthetic seismogram using FWI velocity. Comparing Figure 1(c), the synthetic seismogram from the initial velocity, and 1(d), we can recognize that the synthetic seismogram using FWI velocity, Figure 1(d), resembles the input better than the seismogram using initial velocity. Figure 5 shows the phase residuals between input gather and synthetic seismogram using (a) the initial velocity and (b) the FWI velocity. FWI reduced the phase residual but there are still phase differences as shown in Figure 5(b). It means that convergence is not sufficient yet and further study is needed to improve the convergence.

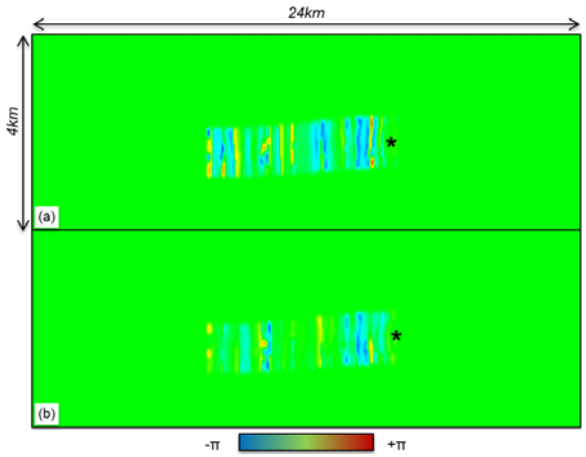

Figure 5. Phase residuals between the input data and the synthetic seismogram using (a) the initial velocity and (b) the FWI velocity against one shot gather in NAZ streamer dataset. The streamer has 6 cables of 7.5 km in length. Shot locations are marked by black asterisks. The green color implies that the phase difference between the synthetic and input seismograms is zero.

Figure 6 displays two Kirchhoff depth migration images using (a) the initial and (b) the FWI velocities. We can recognize that FWI improved the image in the central area below the potential karst zone. Figure 7 compares Kirchhoff depth migration image gathers at the two points denoted by black arrows in Figure 6. Figure 7(a) and 7(b) are image gathers at the location of left arrow in Figure 6 using the velocities (a) before and (b) after FWI. Figure 7(c) and 7(d) are image gathers at the location of right arrow in Figure 6 using the velocities (a) before and (b)

© 2014 SEG

DOI http://dx.doi.org/10.1190/segam2014-1611.1

Downloaded 12/02/14 to 205.196.179.237. Redistribution subject to SEG license or copyright; see Terms of Use at http://library.seg.org/

after FWI. The Kirchhoff gathers become flatter especially below the potential karst zone located around 3 km in depth.

Conclusions

We applied FWI to a deep water NAZ streamer dataset in the Gulf of Mexico where karst features are known to exist. FWI was able to detect the karst area whose existence was interpreted from the depth migration image. The low-velocity anomalies generated by FWI match the Kirchhoff image well. FWI convergence was confirmed by the QC tools of synthetic seismogram and phase difference comparisons. FWI improved Kirchhoff migration image quality and image gather flatness. The phase difference maps show there is further room for improvement of convergence using more advanced algorithm variations.

Acknowledgements

We thank Connie VanSchuyver and Bin Wang for review, Jean Ji and Hao Sun for data preparation. We also thank TGS management for allowing the publication of this study.

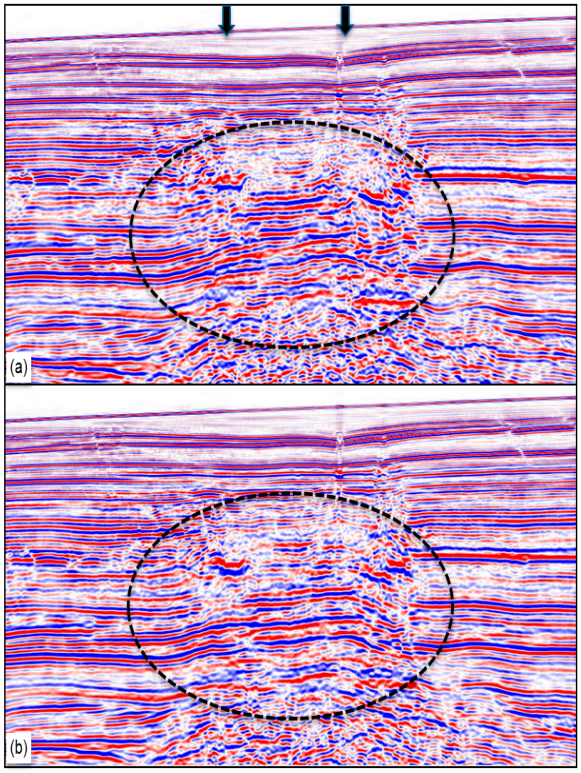

Figure 6. Kirchhoff depth migration images using (a) initial and (b) FWI velocities. Note that FWI improved the image quality in the central area where the karst may exist and also below. Dashed black circle indicates major improvement.

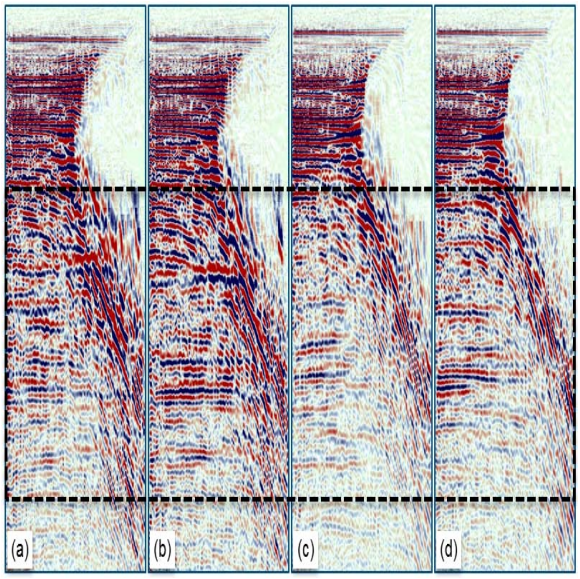

Figure 7. Kirchhoff depth migration image gathers using (a) initial and (b) FWI (c) initial (d) FWI velocities. (a) and (b) are gathers at the location marked by left black arrow in Figure 6. (c) and (d) are gathers at the location marked by right black arrow in Figure 6. The flatness of image gathers was improved after FWI.

© 2014 SEG

DOI http://dx.doi.org/10.1190/segam2014-1611.1

http://dx.doi.org/10.1190/segam2014-1611.1

EDITED REFERENCES

Note: This reference list is a copy-edited version of the reference list submitted by the author. Reference lists for the 2014 SEG Technical Program Expanded Abstracts have been copy edited so that references provided with the online metadata for each paper will achieve a high degree of linking to cited sources that appear on the Web.

REFERENCES

Lailly, P., 1983, The seismic inverse problem as a sequence of before stack migrations: Conference on Inverse Scattering: Theory and Application, SIAM, Proceedings, 206–220.

Pratt, R. G., 1999, Seismic waveform inversion in the frequency domain, Part I: Theory and verification in a physical scale model: Geophysics, **64**, 888–901, http://dx.doi.org/10.1190/1.1444597.

Sheng, J., A. Leeds, M. Buddensiek, and G. T. Schuster, 2006, Early arrival waveform tomography on near-surface refraction data: Geophysics, **71**, no. 4, U47–U57, http://dx.doi.org/10.1190/1.2210969.

Tarantola, A., 1984, Inversion of seismic reflection data in the acoustic approximation: Geophysics, **49**, 1259–1266, http://dx.doi.org/10.1190/1.1441754.

Warner, M., A. Ratcliffe, T. Nangoo, J. Morgan, A. Umpleby, H. Shah, V. Vinje, I. Stekl, L. Guasch, C. Win, G. Conroy, and A. Bertrand, 2013, Anisotropic 3D full-waveform inversion: Geophysics, **78**, no. 2, R59–R80, http://dx.doi.org/10.1190/geo2012-0338.1.

Yoon, K., P. Moghaddam, I. Vlad, M. Warner, and J. Sheng, 2014, Full waveform inversion on Jackdaw ocean bottom nodes data in North Sea: 76th Conference & Exhibition, EAGE, Extended Abstracts, Th E106 11.

Downloaded 12/02/14 to 205.196.179.237. Redistribution subject to SEG license or copyright; see Terms of Use at http://library.seg.org/